The effect of trigonal and tetragonal stresses on the model Jahn-Teller system Y^{2+}:$SrCl_2$

1989 J. Phys.: Condens. Matter 1 10265

(http://iopscience.iop.org/0953-8984/1/51/004)

J. Phys.: Condens. Matter 1 (1989) 10265–10279. Printed in the UK

The effect of trigonal and tetragonal stresses on the model Jahn–Teller system $Y^{2+}:SrCl_2$

H Bill and D Lovy
Department of Physical Chemistry, University of Geneva, 30 Quai E Ansermet, 1211 Genève 4, Switzerland

Received 5 October 1988, in final form 18 August 1989

Abstract. The effect of externally applied stresses of e_g and t_{2g} symmetry on the cubic $E_g \otimes e_g$ Jahn–Teller (JT) system Y^{2+} in $SrCl_2$ is studied. Coupling constants were obtained with the aid of EPR and by relying on a Ham-type cluster JT Hamiltonian, in conjunction with a random strain distribution. This is established from a critical review of the contributing strain sources (including possible percolation effects due to the isotopic composition of natural $SrCl_2$). The stress of t_{2g} symmetry shows strong effects. We conclude that the cubic Ham factor q is nearly one and that the experiments allow, as a function of this latter stress, us to pass gradually towards a trigonal JT effect. The optical absorption spectrum assigned to Y^{2+} is given in addition.

1. Introduction

Random strain plays a very important part in the theory of the weak to intermediate Jahn–Teller effect of the ^2E electronic state, as was first shown by Chase [1] and by Ham [2]. In particular, an adequate interpretation of the ESR spectra of this type of system only became possible when random tetragonal strain was incorporated into the Hamiltonian.

Examples which exhibit in their ESR spectrum pronounced effects due to random strain are Sc^{2+} in the alkaline earth fluorides [3], Y^{2+} [4] and La^{2+} [3] in $SrCl_2$.

However, rather limited use was made, in the published experimental studies, of the fact that stress applied to the sample should likewise have important effects on these systems. Firstly, the experiment will show *if* there is a reaction. Then, information is gained on the distribution and the symmetry of random strains. Finally, by applying stress of different symmetries to the sample one expects to gain information regarding the strength of the dominant JT coupling constant.

These facts prompted us to study the effect of uniaxial stress on the ESR spectrum of an appropriately chosen system. The Y^{2+} ion in $SrCl_2$ is useful because its ESR spectrum is known and has been interpreted successfully [4] with the Ham cluster model. It has the further merit of relative simplicity as we have a $4d^1$ ion with a nuclear spin $I = \frac{1}{2}$. No resolved superhyperfine interaction is seen in this spectrum.

We begin by formulating a few theoretical results. Then, the experiments are described and interpreted with their aid.

0953-8984/89/5110265 + 15 $02.50

2. Structure of the complex; theoretical considerations

Y^{2+} substitutes for a host Sr^{2+} ion in the otherwise locally complete lattice. It is surrounded by a cube of eight Cl^- neighbours. The ground state of the free ion, (^2D), splits in the cubic surroundings (group O_h) into a ^2E_g ground state and a T_{2g} excited state which is located approximately 17450 cm^{-1} above the ground state (see below). Both states are candidates for the JT effect.

2.1. The Jahn–Teller model

According to Herrington *et al* [4] Ham's weak linear $E \otimes \varepsilon$ Jahn–Teller cluster model [2] explains the observed ESR spectra well when one assumes that the vibronic ground-state doublet (^2E_g) and the symmetrical first excited state (a singlet) are separated by an energy difference much larger than the microwave quantum. Then, the use of an effective Hamiltonian within only the doublet is justified in explaining the conventional ESR experiments.

The exact position of the singlet state is not known and we considered whether strain effects arise which involve the ground-state vibronic doublet and this singlet state.

This effective perturbing Hamiltonian is

$$\mathbf{H} = \mathbf{H}_{SE} + \mathbf{H}_{ZE} + \mathbf{H}_{hf} + \mathbf{H}_{ST} \tag{1}$$

as defined in Appendix 1 and in [5].

Herrington *et al* derived the ESR transitions of the Y^{2+} from the Hamiltonian $\mathbf{H}_{SE} + \mathbf{H}_{ZE} + \mathbf{H}_{hf}$ which was evaluated within the ^2E ground vibronic level under the assumptions $\mathbf{H}_{SE} \gg \mathbf{H}_{2E} \gg \mathbf{H}_{hf}$ in second-order perturbation theory. Instead, we prefer to work with the matrix (A1.4) within the vibronic doublet ground state ($|v+\rangle, |v-\rangle$).

Random static strain needs to be included to reconstruct the ESR spectra. It is specified by a strain probability distribution. Tetragonal strain, which is a first-order effect in this model, has a distribution $P(\xi, \varphi)$ which depends on two strain parameters (Appendix 2). In the absence of externally applied stress it is not necessary to know the ξ-dependence of the distribution function to diagonalise the matrix (A1.4), as long as the strain energy differences are large compared with the Zeeman effect [2]. Another reason is that $p(\xi, \varphi) = P(\xi, \varphi)\,\xi\,d\xi\,d\varphi$ tends to zero at the origin for any reasonable strain distribution. Stress applied to the sample changes these facts.

2.2. Random static strain distributions

The form of the probability distribution $P(\xi, \varphi)$ is central to a successful detailed reconstruction of the ESR spectra but, unfortunately, is difficult to assess precisely, as several effects contribute. At present these include:

(i) the intrinsic Frenkel defects of the pure crystal and possible dislocations. In the best of our samples this is probably a minor source;

(ii) usually $SrCl_2$ contains alkali halide ions (K^+, Na^+) [6] as impurities. We used ultrapure powders to begin with and grew the crystals under very clean conditions. Again these contributions are likely to be of minor importance;

(iii) the as-grown crystals contain the yttriums ions in the 3+ state. After x-irradiation they are in part converted into Y^{2+}. Most of the bivalent yttrium ions we observed were of cubic symmetry. In two of the 20 crystals investigated we found in addition a static

Table 1.

	JT ion		
	a	b	Tetrag. centre
g_1	1.9321	1.9291	$g_\parallel = 1.9968$
qg_2	−0.0454	−0.0478	$g_\perp = 1.9234$
A_1	27.7	24.3	$A_\parallel = 18.1$
qA_2	6.45	5.0	$A_\perp = 11.0$

a: this paper.
b: references [3, 4].
hf constants: [10^4 cm^{-1}].

tetragonal Y^{2+} centre. It is seen at 78 K and its spin Hamiltonian parameters (determined with a normal tetragonal spin Hamiltonian) are given in table 1. Thus, possibly, a small percentage of the yttrium ions are locally charge compensated by an interstitial Cl^- ion forming elastic dipoles.

The strain field produced by dislocations decreases as G/r [7]. G contains the orientation, the nature of the dislocation and the angular dependence of the strain field whereas r is the distance to the point where the strain is measured. The strain field induced by point defects is proportional to G'/r^3) [7]. The angular factor G' contains the corresponding factors as above. The charged defects produce, in addition, an electric field gradient, but at present this is not important.

Owing to the JT effect the cubically coordinated Y^{2+} ions contribute in a particular way to the total strain field. According to Englman and Halperin [8] this contribution decays into the lattice approximately as (G''/r^k) with $2 \leqslant k \leqslant 3$. Again G'' contains the angular factors and constants.

The crystals (also the undoped ones) made from very pure starting materials and grown slowly under thoroughly controlled conditions still showed, under a microscope with crossed polarisers, random strain which is much more important than that observed under comparable conditions in the alkaline earth fluorides. Heat treatments resulted in an improvement but did not eliminate this effect totally. This is at variance with respect to the results obtained on equivalently treated alkaline earth fluoride crystals.

One possible origin of this difference is that the natural $SrCl_2$ crystals consist of a random mixture of the two chlorine isotopes, 35 and 37, in the approximate ratio 3 : 1. Thus, each crystal is a random mixture of two isotopic crystals inducing slight misfits which represent sources of random strain. It is probable that the spatial distribution of the isotopes is homogeneous in the sense that a self-similar structure can be constructed under dilatation symmetry from a fixed but arbitrary point of the crystal following the way this is done on a percolating lattice. The crystal can be considered as a three-dimensional net occupied randomly by one of the other of the two isotopes in the probability ratio given above. It thus resembles the percolating structures (e.g. [9]) when for instance ^{37}Cl is considered. This isotope has a probability $p \simeq 0.25$ to occupy a site of this lattice. A Hausdorff dimension d is expected to exist for the crystal according to: mass $\sim r^d$ [10]. The percolation threshold of a three-dimensional FCC lattice is $p_c = 0.2$ [9]. At $p = p_c$ one has $d = 2.5$, whereas $d = 3$ for p close to one. Thus, one has $2.5 < d < 3$, probably of the order of 2.6.

This 'Swiss cheese'-like structure (with respect to each Cl isotope) implies a contribution to the total random strain field which probably has a radial dependence somewhere between r^{-1} and r^{-3}.

Therefore, the total random strain field is expected to decay radially as r^{-n} with $n \leqslant 3$. In Appendix 2 probability distribution functions are considered with reference to the above considerations. We obtain as a useful function (A2.4*a*):

$$P(\xi, \varphi) = \frac{1}{2\pi} \frac{\Lambda}{(\Lambda^2 + \xi^2)^{3/2}} = P(\xi). \tag{2}$$

Another important (though somewhat academic) consequence of the fractal nature of natural $SrCl_2$ crystals is that the optical phonons of the crystal have a fracton-type behaviour similar to the one identified in glasses by Alexander and Orbach [11]. Although the force constant matrix is the same for the two isotopes the masses are different and, depending on the composition of the local cluster, the optical phonon frequencies are then distributed in a manner similar to the one of a (narrow) fracton distribution. This is expected to hold for the distribution of effective frequencies of the ensemble of local JT centres. When only the ground vibronic doublet of the centre is considered this effect results essentially in a distribution of Ham reduction factors. It would certainly be helpful to grow an isotopically pure $SrCl_2:Y^{2+}$ crystal in order to decide about the importance of the above mentioned effects, which finally contribute to the shape of the observed ESR pattern.

3. Experimental

A modified Varian E-line X-band spectrometer was used. Two laboratory built stress cavities were available. A TE_{102} cavity allowed us to work with p parallel to the B-field whereas the one with mode structure TE_{101} always applied stress perpendicular to B. Working temperatures with these cavities were between 1.3 K and room temperature.

The crystals were grown from ultrapure powder (Johnson–Mathey 99.999 pure) in our Bridgman furnace under high vacuum ($<10^{-6}$ Torr, liquid N_2 trap). The melt was contained in a crucible made from ultrapure graphite. The RF induction heating technique was used. The dopant was added to the salt in the form of ultrapure YCl_3 powder (from Johnson-Mathey, London), typically 0.03 to 0.3 %. The resulting cylindrical single crystals (approximately 3 cm length and 15 mm diameter) were cut and ground into oriented slabs of typical dimensions $2.8 \times 5 \times$ (8 to 10) mm. The x-irradiation took place at room temperature (50′, 40 kV/35 mA, Wo-anode).

4. ESR under stress: results

4.1. Tetragonal applied stress

At zero external stress the typical powder-type ESR spectrum is observed, as shown in figure 1, spectrum A. It consists of two patterns due to the hyperfine interaction with the yttrium nucleus ($I = \frac{1}{2}$).

When stress is applied to the sample the spectrum changes dramatically (figure 1, spectrum B, where the effects of the tetragonal stress are seen). We proceed by presenting the different experimentally examined situations in some detail.

4.1.1. $B \parallel p \parallel C_4$ (defined as the z axis). The solutions obtained from matrix A1.4) within this geometry and in the absence of stress, but also under a strong applied tetragonal

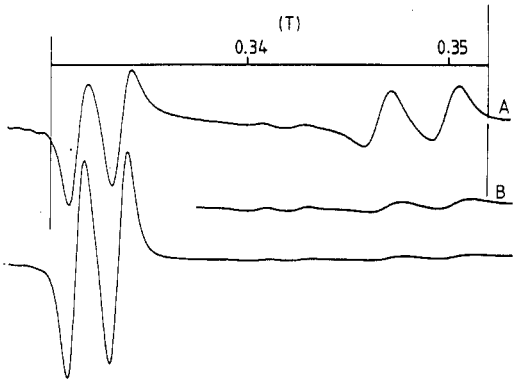

Figure 1. Uniaxial stress experiments with geometry: $p \parallel C_4 \parallel B$. $T = 1.9$ K. Microwave frequency = 9.20451 GHz. A, EPR spectrum observed when $p \simeq 0$; B, Stress $p = 4.35 \times 10^7$ Pa applied. Inset: gain × 4. The two weak central lines are probably due to relative extrema of the powder spectrum (see text).

one, yield two ESR doublets which are centred at $g_1 + qg_2$ for the $|v+\rangle$ vibronic state and $g_1 - qg_2$ for the $|v-\rangle$ one. The separation between the two states is proportional to the applied stress energy, with values $2s$ (A1.3).

As the observed spectrum approaches at highest applied stress the limiting infinite stress situation it is possible to determine with high precision the spin Hamiltonian parameters.

Our values are compared with those of Herrington *et al* [3] in table 1 (left hand part).

The intensity difference between the two line pairs in the experimental ESR spectra, recorded as a function of the applied stress p, allows us to determine the order of the states in the vibronic doublet. Their separation is (from A1.4)

$$2s = 2qV_{SE}(S_{11} - S_{12})p = 2\bar{V}p$$

when the validity of the bulk elastic tensor (**s**, Voigt notation) is assumed. Ligand field theory predicts that $qg_2 < 0$. Thus, from the comparison of these results with the experimental spectra it follows that the state $|v-\rangle$ is lowest and that the proportionality constant $\bar{V}$ is positive. Its value is obtained from the plot $\ln[(n_1/n_0)_p/(n_1/n_0)_0]$ against p where $(n_1/n_0)_p$ is the ratio of the intensity of an experimental line height n_1 over the same quantity of the corresponding calculated one n_0 at pressure p normalised by the zero-pressure ratio. As the transfer of resonating packets from the powder pattern into the two doublets contributes to the intensity changes, a detailed computer simulation of the spectra was necessary. Further, under applied stress the ξ- and φ-dependences of random strain become interrelated because the former quantity shifts the strain distribution away from the origin. The functional form of the strain distribution used in the simulation is given by (2). A grid of values of $\xi_n = n\Delta\xi (n = 0, 1, \ldots, N)$ and $\varphi_m = (2\pi/M)$ $(m = 0, 1, \ldots, M)$ was chosen. At each point the ESR transitions and the associated transition probabilities were obtained from (A1.4). These latter ones were multiplied by $\exp(\pm s/kT)$, and by $p(\xi, \varphi)$. Then, the sum on all the solutions contributing to the (equidistant) magnetic field interval ΔB_k $(k = 1, 2, \ldots, NB$ $(= (B_{max} - B_{min})/\Delta B))$ was evaluated. The numerical procedure followed standard techniques. The stick spectrum was smoothed by convoluting it with a Gaussian line function of half width 2.1 G.

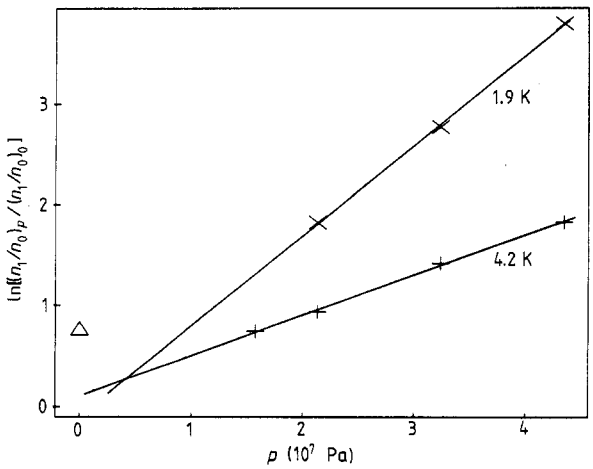

Figure 2. Uniaxial stress applied to the crystal: $p \parallel C_4 \parallel B \parallel z$. For dependence of the line intensities see text. The ratio of the slopes is equal to the inverse ratio of the temperatures.

Each situation consisted of a spectrum calculated with $T = 10000$ K and the corresponding one with $T = 1.9$ K, the temperature of the experiment. Figure 2 shows the plot obtained from the comparison of the two sets. The straight line obtained in this plot is expected within a linear JT effect and under Hook's law. Its slope is

$$\bar{V} = 1.14 \times 10^{-7}\ \mathrm{cm}^{-1}/\mathrm{Pa}.$$

This factor allows the calculation of the reduced coupling constant (qV_{SE}) when the elastic tensor is known. Using the bulk elastic constants of $SrCl_2$ one obtains $qV_{SE} = 6.14 \times 10^3\ \mathrm{cm}^{-1}$/unit strain, where $s_{11} - s_{12} = 1.86 \times 10^{-11}\ \mathrm{m}^2\ \mathrm{N}^{-1}$.

4.1.2. $p \parallel C_4 = z$, $B \parallel C_4 = x$. These experiments give additional information regarding the strain distribution. The solutions of the matrix (A1.4) predict two ESR doublets centred at $g_1 \pm qg_2$ under zero applied stress. Under high stress the doublet associated with the $|v-\rangle$ state is centred at $g_1 - |qg_2/2|$ and the one corresponding to $|v+\rangle$ is at $g_1 + |qg/2|$, by taking the sign of qg_2 as established above. The experimental spectra (figure 3) already exhibit a marked intensity loss of the lines at $g_1 \pm qg_2$ under a comparatively small applied stress. Simultaneously, the set of lines at $g_1 \pm qg_2/2$ increases in intensity: the high-field doublet grows strongly whereas the low-field one is less affected, because the Boltzmann factor favours the $|v-\rangle$ state.

In figure 4 is depicted the intensity (normalised by the zero-stress value) of the lowest field component of the spectrum as a function of applied stress. This plot has been used to adjust the constant of the strain distribution (equation (2)). Its value is $\Lambda = 0{\cdot}69 \times 10^7$.

4.2. Trigonal stress

Trigonal stress is purely off-diagonal within the matrix (A1.4). We have studied its effect experimentally by applying stress along a [111] crystal axis. The main result, common to all of our experiments, is that the pattern decreases strongly in intensity with increasing stress. But neither do the line centres shift within the precision of our measurements nor is any relative intensity change between lines observed. The following situations were investigated.

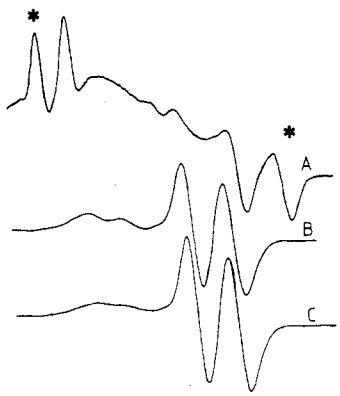

Figure 3. Uniaxial stress applied to the crystal: $p \parallel C_4 \equiv z$, $B \parallel C_4' \equiv x$. $T = 2$ K. A, $p = 0$, the broad feature is due to microphonics and appears when stress is totally released; B, $p = 1.9 \times 10^7$ Pa; C, $p = 2.58 \times 10^7$ Pa.

$p \parallel C_3 \parallel B$. The two ESR doublets are located at $g_1 \pm [(qg_2)^2/2]g_1$ (to second order) at zero stress and both are at g_1 under high stress. Figure 5 (parts (*a*) and (*b*)) gives experimental spectra of this situation. Figure 5(*b*) shows the normalised line intensity as a function of applied stress. Results at 1.9 and 4.2 K sample temperature were used.

$p \parallel C_3$, $B \parallel C_2 \perp C_3$. Figure 6 shows the observed variation of the ESR spectra for this geometry. The stress dependence is the same as that in figure 5(*b*).

No temperature dependence was observed in these experiments within their reproducibility.

Additional stress experiments were performed on $CaF_2 : Sc^{2+}$ to check the generality of the conclusions on other, similar systems involving a weak JT effect. Under the above geometry a strong, full reversible intensity decrease was observed.

On applying tetragonal stress to a suitable $CaF_2 : Sc^{2+}$ sample along C_4 a redistribution of the line intensities was observed analogous to the ones observed on $SrCl_2 : Y^{2+}$. The results from the two systems are fully similar.

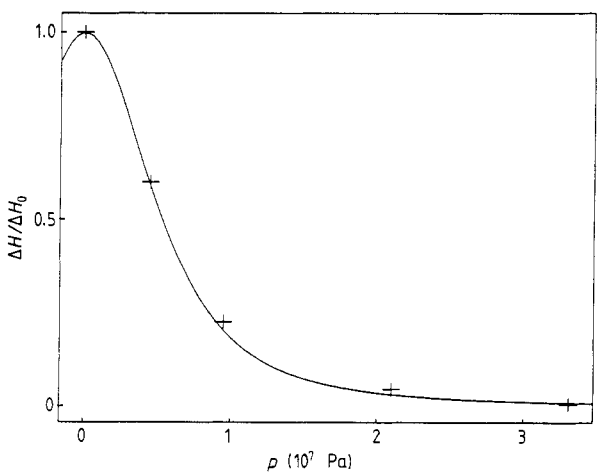

Figure 4. Intensity of the spectral components labelled by an asterisk in figure 3, curve A, as a function of applied stress (same geometry as figure 3). Points, experiment; curve, fit from (A1.4) with distribution equation (2).

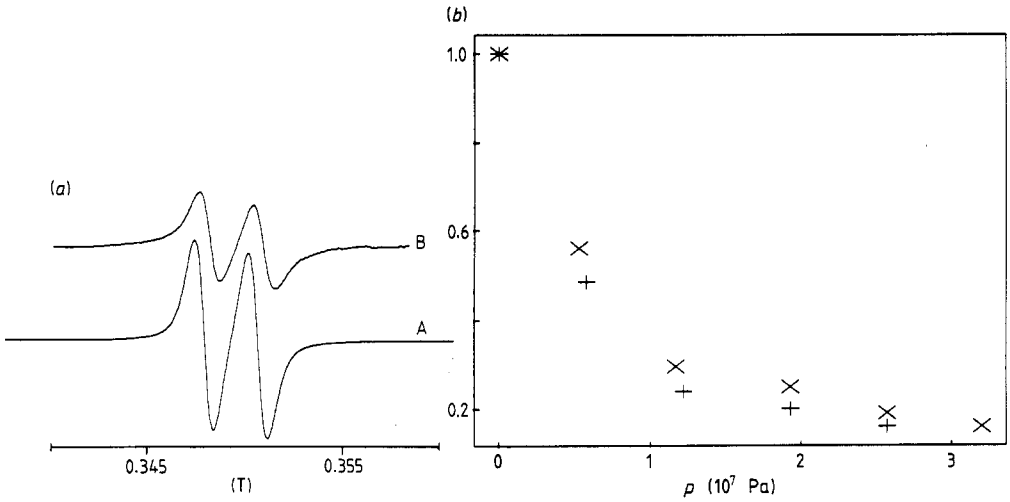

Figure 5. Trigonal stress applied to crystal: $p \parallel B \parallel C_3$. $T = 4.2$ K. Microwave frequency = 9.44467 GHz. (*a*): A, $p = 0$; B, $p = 2.986 \times 10^7$ Pa. (*b*) Peak-to-peak intensity of the low-field line of this spectrum, normalised by its zero-stress value, as a function of p: ×, 1.9 K; +, 4.2 K.

4.3. Temperature dependence

Our simulated ESR spectra obtained for B parallel to C_4 yielded under widely varying conditions a comparatively weak doublet centred at $g = g_1$. Such a doublet is also observed in the experimental spectra. It has been interpreted as being a dynamical feature arising due to partial motional averaging of the powder-type pattern. But it has also been assigned as being due to the excited vibronic singlet state.

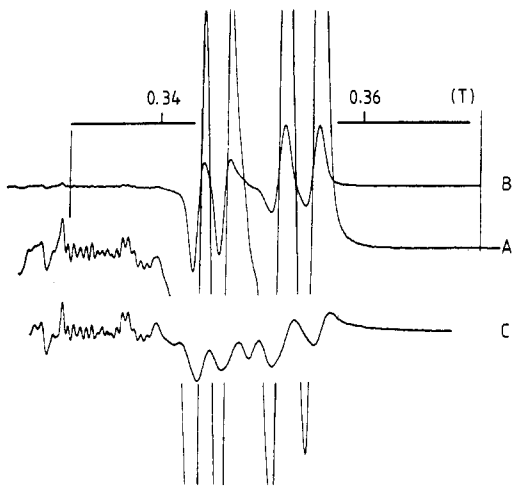

Figure 6. Trigonal stress applied to crystal: $p \parallel C_3$, $B \parallel C_2 \perp C_3$; $T = 1.74$ K; 9.42344 GHz. A, $p = 0$; B, same as A except gain ÷ 10; C, $p = 2.51 \times 10^7$ Pa. The structure below 0.34 T is due to static impurities introduced to show that the effect is genuine to Y^{2+}.

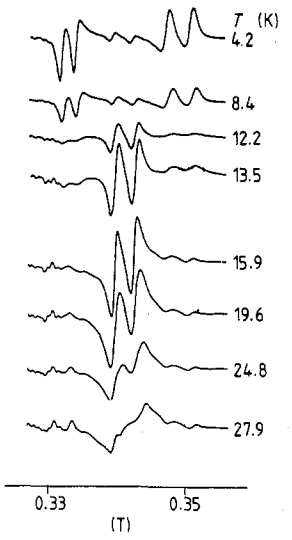

Figure 7. Temperature dependence of the EPR spectrum at zero external stress. $B \parallel C_4$. T (K).

Figure 7 shows the temperature dependence of the ESR spectrum. It shows clearly that there is a motionally averaged component present. On the other hand, a small contribution due to stationary points generated by the internal strain distribution is also present as can be seen in figure 1, curve B. This central doublet is unaffected by temperature between 4.2 and 1.5 K.

On the other hand it is more unlikely that one of the excited vibronic singlets contributes because we did not observe any effect on the central doublet due to non-diagonal external strain matrix elements in our stress experiments, between 15 and 35 K.

5. Optical absorption spectrum

A few optical absorption experiments have been performed (with a Beckman Dk 2a spectrometer) on our x-rayed samples.

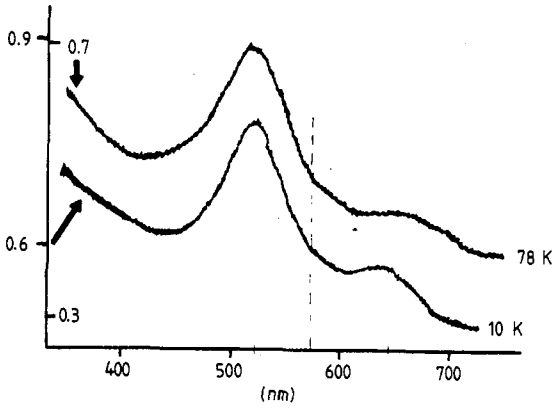

Figure 8. Optical absorption spectrum of Y^{2+}: $SrCl_2$. $T = 78$ K, ordinate values right-hand scale; $T = 10$ K, ordinate values left-hand scale.

The ones containing Y^{2+} exhibited a characteristic pink colouration and the absorption band (of intermediate oscillator strength) shown in figure 8 was found. Its optical density is proportional to the Y^{2+} ion concentration.

As shown by figure 8 the shape of the absorption band is temperature dependent. This fact and the peculiar shape are reminiscent of the structure and temperature dependence of optical transitions of JT states, as theoretically predicted by several authors.

For these reasons we tentatively assign the band to transitions between the Jahn–Teller active E_g ground state and T_{2g} excited state of the Y^{2+} ion. The centre of the structure is at 17455 cm^{-1}.

6. Discussion and conclusions

(i) Effect of trigonal strain. This remarkable effect indicates that coupling to trigonal vibrations is not much smaller than that to tetragonal ones. An attempt to simulate the intensity decrease shown in figure 5(*c*) with the aid of the model, matrix (A1.4), by including the term (A1.1*d*), did not yield satisfactory results. The observed intensity decrease of the ESR pattern was obtained, but in conjunction with sizeable shifts of the resonance fields, in disagreement with experiment.

A useful discussion has to consider, probably, the transition between a cubic and a trigonal (D_{3d} symmetry) Jahn–Teller effect. We sketch in the following the model by neglecting the tetragonal random-strain effects.

It is appropriate to discuss this situation with respect to trigonal axes ($Z \| [111]$, $Y \| [1\bar{1}0]$, $X \| [\bar{1}\bar{1}2]$). Within the weak coupling JT model one still has in the limit of cubic symmetry a vibronic $E \times D_{1/2} = \Gamma_8$ ground state. The electronic basis involved is formed by states given by

$$|E\theta\rangle = \cos\gamma|X^2 - Y^2\rangle + \sqrt{8}\sin\gamma|XZ\rangle$$
$$|E\varepsilon\rangle = \sqrt{8}\sin\gamma|YZ\rangle - 2\cos\gamma|XY\rangle$$

where $\gamma = \gamma_0 = \cos^{-1}3^{-1/2}$ for cubic symmetry. Applying now stress along [111] amounts to creating a trigonal field which modifies the value of γ. As the stress-induced trigonal field is probably small compared with the cubic field splitting Δ, the value $\gamma - \gamma_0$ remains small.

One has to go to the combined effect (trigonal field + spin–orbit coupling (A1.1*d*) to obtain an operator which splits the Γ_8 state under D_{3d} symmetry. Expressed in trigonal axes this gives

$$\mathbf{H}_t = kpS_Z\mathbf{u}_2 \tag{3}$$

with k containing the factors not important for the discussion. The matrix $\mathbf{u}_2$ has the form given in Appendix 1, but it refers to the trigonal axes. This term produces modified selection rules of the ESR transitions as it modifies the admixture of the two electronic states involved in the vibronic doublet. The lengthy detailed analysis will be given elsewhere.

This discussion shows that a trigonal strain which is not sufficiently quenched by the cubic $E \otimes e$ JT effect is at the origin of the modified selection rules observed in the ESR spectrum. If it were strong enough it would probably totally impose a trigonal JT effect.

(ii) Influence of totally symmetrical a_1 stress. Stress applied along [111] transforms under cubic symmetry as $a_{1g} + t_{2g}$. Thus, there might result a contribution from a_{1g} stress through coupling with other irreducible representations (IREP) modes. Cross terms between the vibrations transforming as e_g and those transforming as a_{1g} probably affect most importantly the frequency of the effective JT mode. This amounts to a systematic shift of the effective e mode frequency.

Therefore, the weak cubic JT effect, probably in conjunction with the cubic geometry, is probably the origin of the strong effects due to external trigonal stress. Note that the local deformation mode pair transforming as e_g corresponds to a tangential movement with respect to the bonds Y^{3+}—Cl^- whereas the trigonal deformation coordinates of one of the t_{2g} modes involve radial displacements.

Acknowledgments

This work was supported by the Swiss National Sciences Foundation. The authors acknowledge the help of V Monico and A Gerber for crystal growth, of F Rouge for mechanical construction work and J P Plüss for the realisation of the interfaces between the spectrometer and the computer, and Renata Da Costa for typing the manuscript.

Appendix 1. JT model of the lowest vibronic states

This appendix gives the results obtained from the Jahn–Teller theory which are needed in the main text. The theory of the weak coupling Jahn–Teller effect between an orbital E_g doublet and an effective local cluster mode transforming likewise as ε_g (cubic symmetry) has been published by Ham [2].

We have followed the notation of [5] and use Greek lower case letters for the IREP of vibrations.

The two states of the vibronic ground-state doublet are written $\{|E\upsilon\rangle, |E\upsilon\rangle\}$. The perturbing effective Hamiltonian which acts within this doublet contains, in decreasing order:

(i) Tetragonal strain (V_E = coupling constant, e_θ and e_ε are the tetragonal components of the strain tensor)

$$\mathbf{H}_{SE} = V_E(e_\theta \mathbf{u}_\theta + e_\varepsilon \mathbf{u}_\varepsilon) \tag{A1.1a}$$

(ii) Electronic Zeeman term (g_1, g_2 are the g-values within the electronic doublet)

$$\mathbf{H}_{ZE} = g_1\beta_0 \boldsymbol{B}\cdot\boldsymbol{S}\mathbf{u}_1 + \tfrac{1}{2}g_2\beta_0[(3B_zS_z - \boldsymbol{B}\cdot\boldsymbol{S})\mathbf{u}_\theta + \sqrt{3}(B_xS_x - B_yS_y)\mathbf{u}_\varepsilon]. \tag{A1.1b}$$

(iii) Hyperfine interaction: ($I = \frac{1}{2}$, A_1 and A_2 are the hyperfine constants within the electronic doublet)

$$\mathbf{H}_{hf} = A_1\boldsymbol{S}\cdot\boldsymbol{I}\cdot\mathbf{u}_1 + \tfrac{1}{2}A_2[(3S_2I_2 - \boldsymbol{S}\cdot\boldsymbol{I})\mathbf{u}_\theta + \sqrt{3}(S_xI_x - S_yI_y)\mathbf{u}_\varepsilon]. \tag{A1.1c}$$

(iv) Trigonal strain in second order in conjunction with the spin–orbit coupling (V_T = coupling constant, e_{xy} etc = trigonal components of the strain tensor, λ = the spin–orbit

coupling constant, Δ = the cubic field splitting between the electronic E_g ground state and the T_{2g} excited state).

$$\mathbf{H}_{ST} = (\lambda V_T/\Delta)(S_x e_{yz} + S_y e_{zx} + S_z e_{xy})\mathbf{u}_2 \tag{A1.1d}$$

Finally

$$\mathbf{u}_1 = \begin{pmatrix} 1 & 0 \\ 0 & 1 \end{pmatrix} \qquad \mathbf{u}_2 = p\begin{pmatrix} 0 & -i \\ i & 0 \end{pmatrix} \qquad \mathbf{u}_\varepsilon = q\begin{pmatrix} -1 & 0 \\ 0 & 1 \end{pmatrix} \qquad \mathbf{u}_\theta = q\begin{pmatrix} 0 & 1 \\ 1 & 0 \end{pmatrix}$$

within the vibronic doublet. The numbers p and q are the Ham reduction factors as defined in [2].

Keeping the spin-dependent parts as operators one obtains a 2×2 matrix within the unperturbed vibronic ground level. It is useful to diagonalise first $\mathbf{H}_{SE}$ and to transform the other perturbations to the thus obtained basis functions. To this end the tetragonal strain is expressed in polar coordinates. The following quantities are used:

$$\xi^2 = (e_\theta^2 + e_\varepsilon^2) \quad \text{and} \quad \tan\varphi = e_\varepsilon/e_\theta. \tag{A1.2}$$

The matrix

$$\mathbf{S} = \begin{pmatrix} \sin\tfrac{1}{2}\varphi & \cos\tfrac{1}{2}\varphi \\ \cos{}^*\varphi & -\sin\tfrac{1}{2}\varphi \end{pmatrix}$$

diagonalises $\mathbf{H}_{SE}$:

$$\mathbf{H}'_{ES} = \mathbf{S}\mathbf{H}_{SE}\mathbf{S}^{tr} = qV_{SE}\mathbf{u}_\theta = s\mathbf{u}_\theta \tag{A1.3a}$$

with basis functions

$$\begin{aligned} |v+\rangle &= \sin\tfrac{1}{2}\varphi\,|E_\theta v\rangle + \cos\tfrac{1}{2}\varphi\,|E_\varepsilon v\rangle \\ |v-\rangle &= \cos\tfrac{1}{2}\varphi\,|E_\theta v\rangle - \sin\tfrac{1}{2}\varphi\,|E_\varepsilon v\rangle. \end{aligned} \tag{A1.3b}$$

The ESR transitions are obtained by writing out the spin part within the product space $E_g v \times D(S) \times D(I)$). This is a standard procedure and the details are not given. The matrix (A1.4) contains the necessary information.

$$\begin{bmatrix} |v+\rangle & |v-\rangle \\ qV_E\xi + g_1\beta_0 \boldsymbol{B}\cdot\boldsymbol{S} + A_1\boldsymbol{I}\cdot\boldsymbol{S} + \tfrac{1}{2}q[g_2\beta_0(3B_zS_z - \boldsymbol{B}\cdot\boldsymbol{S}) + A_2(3I_zS_z - \boldsymbol{I}\cdot\boldsymbol{S})]\cos\varphi + \tfrac{1}{2}q\sqrt{3}[g_2\beta_0(B_xS_x - B_yS_y) + A_2(I_xS_x - I_yS_y)]\sin\varphi & -\tfrac{1}{2}q[g_2\beta_0(3B_zS_z - \boldsymbol{B}\cdot\boldsymbol{S}) + A_2(3I_zS_z - \boldsymbol{I}\cdot\boldsymbol{S})]\sin\varphi + \tfrac{1}{2}q\sqrt{3}[g_2\beta_0(B_xS_x - B_yS_y) + A_2(I_xS_x - S_yI_y)]\cos\varphi \\ \text{CC} & -qV_E\xi + g_1\beta_0\boldsymbol{B}\cdot\boldsymbol{S} + A_1\boldsymbol{I}\cdot\boldsymbol{S} - \tfrac{1}{2}q[g_2\beta_0(3B_zS_z - \boldsymbol{B}\cdot\boldsymbol{S}) + A_2(3I_zS_z - \boldsymbol{I}\cdot\boldsymbol{S})]\cos\varphi - \tfrac{1}{2}q\sqrt{3}[g_2\beta_0(B_xS_x - B_yS_y) + A_2(I_xS_x - I_yS_y)]\sin\varphi \end{bmatrix} \tag{A1.4}$$

Appendix 2. Random strain, distribution function

The aim of this appendix is to establish a suitable strain distribution function. We choose a homogenous random distribution of strain sources, assumed to be mutually uncorrelated. Their density is $\rho = N/V$. The strain field produced by each of them is assumed to have the form given by

$$e'_{ik}(Z) = \frac{c}{r^n}\left(\delta_{ik} - \frac{x_i x_k}{r^2}\right) = e'_{ik}(\boldsymbol{r}) \tag{A2.1}$$

with $1.5 \leqslant n \leqslant 3$, where c contains the strength and the nature of the local strain source, labelled Z, at position $\boldsymbol{r} = (x_1, x_2, x_3) = (r, \vartheta, \varphi)$ with respect to the origin chosen to be the point where the total strain is measured. As we are interested in the functional dependence of the probability distribution we do not try to to develop a model for c. The angular dependence of (A2.1) was essentially chosen for mathematical convenience. Indeed, it is of great use in handling radial divergency problems in (A2.4). The probability distribution of the sources is $p(Z)$.

The strain tensor is assumed to be symmetric. The two linear combinations of elements (A2.1) which transform as a basis of the IREP E_g in O_h symmetry are represented by the symbols $e'_\theta(\boldsymbol{r}), e'_\varepsilon(\boldsymbol{r})$ (see § 3.3.4 of [7], which treats the general subject in detail).

Under these assumptions the strain distribution function $P(e_\theta, e_\varepsilon)$ is given by the weighted average over the occurrence of pairs of global strains arising from the randomly distributed sources. The approximate form is (we replace the sum by an integral and assumed the validity of Hook's law).

$$P(e_\theta, e_\varepsilon) = \int \mathrm{d}Z\, p(Z)\delta(e_\theta - e'_\theta(Z))\delta(e_\varepsilon - e'_\varepsilon(Z)). \tag{A2.2a}$$

This integral is transformed with the aid of the spectral representation of the δ-function and then further transformed according to [12, 7], to give

$$P(e_\theta, e_\varepsilon) = \frac{1}{(2\pi)^2}\int\int \mathrm{d}x\,\mathrm{d}y\,\exp[\mathrm{i}(xe_\theta + ye_\varepsilon)]\exp(-\rho J(x, y)). \tag{A2.2b}$$

This last integral assumes that $N \to \infty$ with constant density of defects. Thus, $p(Z)\,\mathrm{d}Z$ is proportional to the volume. Transforming to polar coordinates with respect to r one has $p(Z)\,\mathrm{d}Z = r^2 \sin\vartheta\,\mathrm{d}\vartheta\,\mathrm{d}\varphi$.

The quantity $J(x, y)$ has the following form [7]:

$$J(x, y) = \int \mathrm{d}Z\, p(Z)\{1 - \exp[-\mathrm{i}(xe'_\theta(\boldsymbol{r}) + ye'_\varepsilon(\boldsymbol{r})]\}. \tag{A2.3}$$

We replace $p(Z)\,\mathrm{d}Z$ as given above and introduce the explicit form of e'_θ and e'_ε with the aid of (A2.1). Additionally, it is useful to transform the dummy variables x, y (also in the Fourier integral (A2.2)) to polar coordinates ($x = \sigma\cos\alpha$, $y = \sigma\sin\alpha$). One obtains after some further changes of variables ($t = r^{-n}$, $t_1 = R_1^{-n}$, $t_2 = R_2^{-n}$, with $R_1 \ll R_2$)

$$J(\sigma, \alpha) = \frac{1}{n}\int\int \mathrm{d}\Omega \int_{t_2}^{t_1} \mathrm{d}t\, t^{-\mu}(1 - \mathrm{e}^{-\mathrm{i}agt}) \tag{A2.4}$$

where $d\Omega =$ the angular part of the polar volume element and $g = \cos\alpha(1 - 3\cos\vartheta) - \sqrt{3}\sin\alpha\sin^2\vartheta\cos 2\varphi$. Furthermore, $\mu = (3+n)/n$ and $a = 3c\sigma/2$.

As discussed in the main text a possible range of n values is $1.5 < n < 3$ which implies $2 \leqslant \mu \leqslant 3$.

An energy perturbation decaying as r^{-3} or slower diverges as $r \to \infty$. Its angular dependence is such, at present, that it can force the expression to converge. For this reason the t-integral of (A2.4) needs careful consideration regarding its convergence properties [7, 12].

(a) $\mu = 2$

The radial integral is evaluated by integrating by parts. The angular integral of g ensures convergence of the imaginary part.

The angular integral yields finally: $(u = \sin^2(\vartheta/2))$

$$J(\sigma, \alpha) = 4c\,\pi\sigma\cos\alpha \int du\,[AH\tfrac{1}{2}(\pi - 2\cos^{-1}(AH/BH)) + BH\sin(\cos^{-1}(AH/BH))] \tag{A2.5}$$

with $AH = 6u(1-u) - 1$ and $BH = 2\sqrt{3}(\tan\alpha)u(1-u)$. Furthermore $u_1 = 0$, $u_2 = 1$ for $0 \leqslant \alpha < 30°$, and $u_{2,1} = \frac{1}{2} \pm \frac{1}{2}[(\cot\alpha + \sqrt{3})/(3\cot\alpha + \sqrt{3})]^{1/2}$ for $\alpha \geqslant 30°$.

This integral depends very little on α and we assume it to be constant (= Const) with respect to this variable in what follows. Apart from this result, its exact value is of no interest, as we decided not to develop a detailed model for c. Thus

$$J(\sigma, \alpha) = (\text{Const})\sigma$$

(b) $2 < \mu < 3$

The radial part yields

$$= -\left(\frac{3c\sigma}{2}\right)^{\mu-1} |g|^{\mu-1}\left\{\Gamma(\mu-1)\cos\pi(1-\mu)/2 + \frac{\mathrm{i}^{\mu+1}}{2}[(-1)^{\mu}\Gamma(1-\mu, -\mathrm{i}a|g|t_2) + \Gamma(1-\mu, \mathrm{i}a|g|t_2]\right\}. \tag{A2.6}$$

The $\Gamma(1-\mu, \mathrm{i}a|g|t)$ are incomplete gamma functions of imaginary argument. The angular integral of this expression is obtained without special difficulties for the real part, whereas the imaginary part needs a detailed analysis, beyond the scope of the present paper. However, $J(\ ,\ ) \sim \sigma^{\sigma-1}$.

(c) $\mu = 3$

The t-integral yields

$$= \tfrac{3}{4}c^2\sigma^2 g^2\left(1 + \tfrac{3}{4}\ln\frac{R_1}{R_2}\right) + \mathrm{i}\left(c\sigma g\frac{1}{t_2} - \tfrac{3}{4}c^2\sigma^2\pi g|g|\right). \tag{A2.7}$$

The angular integral results in:

$$\tfrac{12}{5}\,c^2\sigma^2\pi\left(1 + \tfrac{3}{4}\ln\frac{R_1}{R_2} - \frac{\mathrm{i}}{2}\int\int d\Omega\, g|g|\right).$$

The real part is independent of α. Its logarithmic divergence arises because the finite lattice sum was replaced by (A2.2). When the finite lattice sum is retained the result remains finite. The first term of the imaginary part is forced to zero by the angular integral and the second one becomes very small in its absolute value compared with the real part. Making the further approximation to neglect it we are led to the result.

$$J(\sigma, \alpha) = (\text{Const})\sigma^2.$$

Again, we are not interested in the exact value of the integral—as long as it is (nearly) independent of σ and is finite.

Introducing these results into (A2.2), using polar coordinates (A1.2) to transform e_θ, e_ε, and integrating over α one finds

$$P(\xi, \varphi) = \frac{1}{2\pi}\int_0^\infty \mathrm{d}\sigma\, \sigma J_0(\xi\sigma)\exp[-(\text{Const})\sigma^m] \tag{A2.8}$$

where $J_0(\xi\sigma)$ is a Bessel function of order zero and $m = 3/n$. We looked for solutions both for $m = 1$ and 2. They are:

$$P(\xi, \varphi) = \frac{1}{2\pi}\frac{\Lambda}{(\Lambda^2 + \xi^2)^{3/2}} = P(\xi) \qquad \text{for } n = 3 \quad (m = 1) \tag{A2.8a}$$

$$P(\xi, \varphi) = \frac{1}{\Lambda\sqrt{\pi}}\exp[-(\xi/2\Lambda)^2] = P(\xi) \qquad \text{for } n = 1.5 \quad (m = 2). \tag{A2.8b}$$

The parameter Λ contains the result of the integrations which do not depend on ξ. It is treated in what follows as an adjustable parameter.

The interesting result is that for point-like dipolar strain sources ($n = 3$) the distribution is not a Gaussian.

We used both distributions to fit our experimental spectra. (A2.8*a*) gave somewhat better results and was for this reason used.

References

[1] Chase L L 1968 *Phys. Rev.* A **168** 341
[2] Ham F S 1965 *Phys. Rev.* A **138** 1727
[3] Herrington J R, Estle T L and Boatner L A 1971 *Phys. Rev.* B **3** 2933
[4] Herrington J R, Boatner L A, Aton T J and Estle T L 1974 *Phys. Rev.* B **10** 833
[5] Bill H 1984 *The Dynamical Jahn–Teller Effect in Localised Systems* ed. Yu E Perlin and M Wagner (Amsterdam: Elsevier) ch 13
[6] De Siebenthal J M and Bill H 1977 *Phys. Status Solidi* b **79** 259
[7] Stoneham A M 1969 *Rev. Mod. Phys.* **41** 82
[8] Englman R and Halperin B 1978 *Ann. Phys., NY* **3** 453
[9] Zaller R 1983 *The Physics of Amorphous Solids* (New York: Wiley)
[10] Mandelbrot B 1982 *The Fractal Geometry of Nature* (San Francisco: Freeman)
[11] Alexander S and Orbach R 1984 *J. Physique lett.* **45** L1155
[12] Grant W J C and Strandberg M W P 1964 *Phys. Rev.* **135** A715